Title

Unlocking the Catalytic Potential of TiO2-Supported Pt Single Atoms for the Reverse Water-Gas Shift Reaction by Altering Their Chemical Environment.

Journal

JACS Au, 1(7)

Authors

Chen, Linxiao

Unocic, Raymond

Hoffman, Adam

et al.

Publication Date

2021-07-26

DOI

10.1021/jacsau.1c00111

Peer reviewed

JACS Au
AN OPEN ACCESS JOURNAL OF THE AMERICAN CHEMICAL SOCIETY

pubs.acs.org/jacsau

Article

Unlocking the Catalytic Potential of TiO_2-Supported Pt Single Atoms for the Reverse Water–Gas Shift Reaction by Altering Their Chemical Environment

Linxiao Chen, Raymond R. Unocic, Adam S. Hoffman, Jiyun Hong, Adriano H. Braga, Zhenghong Bao, Simon R. Bare, and Janos Szanyi*

Cite This: *JACS Au* 2021, 1, 977–986

Read Online

ACCESS | Metrics & More | Article Recommendations | Supporting Information

ABSTRACT: Single-atom catalysts (SACs) often exhibit dynamic responses to the reaction and pretreatment environment that affect their activity. The lack of understanding of these behaviors hinders the development of effective, stable SACs, and makes their investigations rather difficult. Here we report a reduction–oxidation cycle that induces nearly 5-fold activity enhancement on Pt/TiO_2 SACs for the reverse water–gas shift (rWGS) reaction. We combine microscopy (STEM) and spectroscopy (XAS and IR) studies with kinetic measurements, to convincingly show that the low activity on the fresh SAC is a result of limited accessibility of Pt single atoms (Pt_1) due to high Pt–O coordination. The reduction step mobilizes Pt_1, forming small, amorphous, and unstable Pt aggregates. The reoxidation step redisperses Pt into Pt_1, but in a new, less O-coordinated chemical environment that makes the single metal atoms more accessible and, consequently, more active. After the cycle, the SAC exhibits superior rWGS activity to nonatomically dispersed Pt/TiO_2. During the rWGS, the activated Pt_1 experience slow deactivation, but can be reactivated by mild oxidation. This work demonstrates a clear picture of how the structural evolution of Pt/TiO_2 SACs leads to ultimate catalytic efficiency, offering desired understanding on the rarely explored dynamic chemical environment of supported single metal atoms and its catalytic consequences.

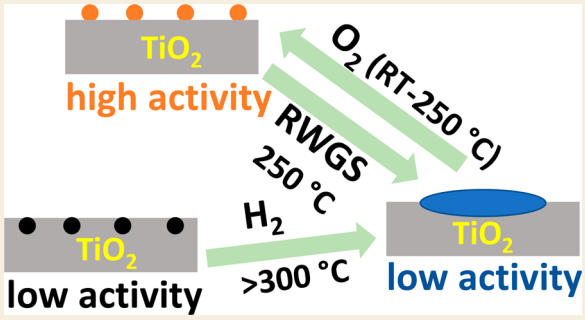

KEYWORDS: *single-atom catalyst, CO_2 hydrogenation, reverse water–gas shift, platinum, titania*

INTRODUCTION

The hydrogenation of CO_2 to CO, also known as the reverse water–gas shift (rWGS), has sparked research interests from various perspectives. First, it responds to the call for effective carbon mitigation technologies, with the bonus of producing value-added chemicals.[1,2] In addition, it is a mechanistic proxy to understanding the hydrogenation of organic feedstocks containing C═O functional groups, many of which are also intriguing processes.[3−5] Furthermore, its reverse reaction, the water–gas shift, has significant applications in hydrogen production and tuning syngas composition, and thus plays indispensable roles in the global economy.[6,7] Previous studies established that on supported noble metal catalysts, the CO selectivity increases as the particle size decreases.[8−10] Meanwhile, the active sites are proven to be at the metal-oxide interface, created by the hydroxylation of the M–O bonds.[11,12] These findings inspired our interests in studying single-atom catalysts (SACs) for the rWGS, as they are logically the ideal catalysts with the optimal selectivity, activity, and site uniformity for mechanistic investigations.

The recent exploding interests in noble metal SACs are driven by the pursuit of ultimate metal utilization efficiency and superior selectivity originating from metal site uniformity.[13−15] Despite the ample volume of literature, SACs are rarely explored for high-temperature (>150 °C) hydrogenation reactions, such as the rWGS.[16,17] This is partially due to their dynamic structures under such conditions: on oxide supports, metal single atoms are mainly stabilized by M–O bonds, and thus the interruption of such bonds by harsh reducing conditions often mobilizes them, inducing structural changes of the SACs. These behaviors have been shown to impact the activity of SACs, and also sparsely identified under oxidizing conditions.[18−20] Not only does the lack of understanding of processes taking place in SACs under reaction and pretreatment conditions limit the application scope of SACs it also hinders the precise understanding of the nature of active sites and the chemistry occurring on them. In addition to the

Received: March 9, 2021
Published: June 4, 2021

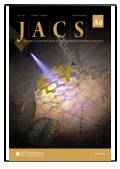

https://doi.org/10.1021/jacsau.1c00111
JACS Au 2021, 1, 977–986

dynamic nature of SACs, the metal−support interaction (MSI) is another underexplored topic in single-atom catalysis. Unlike in supported metal nanoparticle catalysts, the chemical environment of metal single atoms is mostly determined by their bonding with the support. Therefore, MSI in SACs often has profound impacts,[10,21,22] reminiscent of the significant influences that ligands cast on metal centers in homogeneous catalysts. In addition, it has been shown that the nature of MSI may change when atomic metal dispersion is reached.[23,24] Therefore, understanding the role of MSI in the modulation of the activity and selectivity of SACs is critical.

In this work, we investigated Pt/TiO_2 (anatase) SACs for the rWGS. We show that the potential of Pt single atoms (Pt_1) to carry out the catalytic transformation is initially concealed by their saturated coordination with TiO_2, and can be unlocked by a reduction−oxidation treatment. Through a combination of kinetic, spectroscopic, and microscopic evidence, we illustrate that controlled reducing atmosphere mobilizes Pt_1, forming small, amorphous aggregates that can be redispersed into Pt_1 by mild oxidation. The redispersed Pt_1 shows less coordination with surface O than Pt_1 of the fresh catalyst, and thus better accessibility, and consequently higher activity in the rWGS reaction. Although the activated Pt_1/TiO_2 deactivates slowly during the rWGS reaction, the activity is fully recoverable by mild oxidation. Therefore, this work provides a strategy to properly alter the chemical environment of metal single atoms to achieve ultimate catalytic efficiency. This study also offers fundamental understanding on the structural evolution of SACs under various conditions and how these events determine the catalytic activity.

RESULTS

1. Activating Pt Single Atoms (Pt_1) by a Reduction−Oxidation (Red_Ox) Cycle

We synthesized three Pt/TiO_2 catalysts to test for the rWGS. Small anatase particles were chosen as the support because the method for preparing Pt/TiO_2 single-atom catalysts (SAC) is available with this phase.[25] The anatase support is stable at ≤800 °C, as no phase transformation was observed after calcination at such temperatures (Figure S1), a result of the small particle size.[26,27] Therefore, any changes in the activity of these catalysts cannot be caused by support phase changes. Two catalysts were prepared by the strong electrostatic adsorption method with Pt loading of 0.025 wt %. Because of the large difference in the surface areas of the TiO_2 used for the preparation (~180 and ~20 m^2/g, Table S1), the resulting materials contain exclusively Pt single atoms (Pt_1/TiO_2) and subnanometer Pt clusters (Pt_n/TiO_2, d = 0.56 ± 0.06 nm, Figure S2a−c, along with Pt single atoms), respectively. The third catalyst, 2 wt % Pt/TiO_2, was prepared with the incipient wetness impregnation method and contains Pt nanoparticles (Pt NP/TiO_2, d = 1.0 ± 0.2 nm, Figure S 2d). After calcination in air at 400 °C, the "fresh" catalysts were obtained. The atomic dispersion of Pt on the fresh Pt_1/TiO_2 was confirmed by high-angle annular dark-field scanning transmission electron microscopy (HAADF-STEM), X-ray absorption spectroscopy (XAS), and CO-probe IR (CO-IR), which will be discussed in detail in the next section (Figures 3−5).

All three Pt/TiO_2 catalysts tested for the rWGS show 100% CO selectivity at 250 °C. Surprisingly, Figure 1a shows that Pt_1/TiO_2, expected to have the most interfacial active sites and hence the highest activity per Pt,[11,12] is not as active as Pt_n/TiO_2. Meanwhile, it exhibits a minor (~50%) rate increase in 3 h, which is absent for the other two catalysts. The unexpected low rWGS rate and the slight activation under the reducing rWGS atmosphere led to the hypothesis that Pt_1/TiO_2 requires activation by appropriate reduction treatment. Therefore, we treated Pt_1/TiO_2 with H_2 at 500 °C for 1 h (H500−1h, reduction conditions below labeled similarly), before testing it for the rWGS at 250 °C. Figure 1b shows that the H500-1h reduction alone does not lead to meaningful rate increase (first group, blue bar), but after reoxidizing H500-1h Pt_1/TiO_2 with air at 250 °C, the rate (red bar) becomes nearly 3-fold that of the fresh catalyst, i.e., Pt_1/TiO_2 is drastically activated by the applied reduction−oxidation (referred herein as Red_Ox) cycle. The reoxidation step can be partially achieved under very mild conditions, by room-temperature air exposure for several days (purple bar). In addition, reoxidizing Pt_1/TiO_2 used in 250 °C rWGS for 13 h (R250-13h) also leads to the activation (second group), indicating that the rWGS reaction is equivalent to a reduction step. In contrast, the Red_Ox cycle has a negligible activation effect on Pt_n/TiO_2 or Pt NP/TiO_2 (last two groups), suggesting that this process selectively activates Pt_1 but not other Pt species (clusters or nanoparticles).

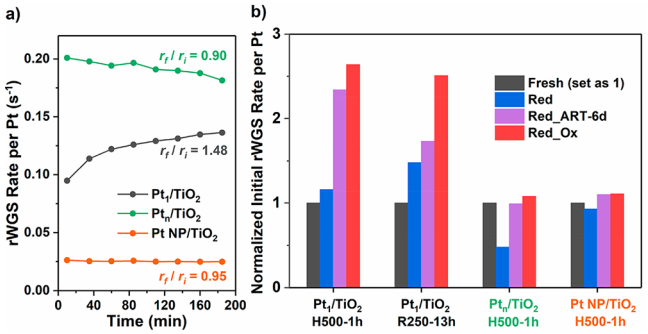

Figure 1. Comparing Pt single atoms (Pt_1), small clusters (Pt_n), and nanoparticles (Pt NP) supported on anatase TiO_2 for the rWGS catalysis. (a) Variations in the per-Pt reaction rate with time-on-stream. (b) Changes in the initial rate (t = 10 min) after a reduction−oxidation cycle. In each group, the black, blue, purple, and red bars represent the fresh sample, after reduction (H_2, 500 °C, 1 h, H500-1h, or the rWGS reaction, 250 °C, 13 h, R250-13h), partial oxidation (air, room temperature, 6 days), and complete oxidation (air, 250 °C, 3 h), respectively. Each group was normalized to the fresh catalyst to emphasize the changes. Reaction conditions: 30 mg catalysts, H_2:CO_2:He = 4:1:15, total flow = 40 SCCM, T = 250 °C, CO_2 conversion <2%. The CO selectivity is 100% in all cases.

We varied the reduction condition to systematically examine its impacts on Pt_1 activation and maximize the catalytic efficiency of Pt_1/TiO_2. Red bars in Figure 2a show the initial reaction rate (at 10 min time-on-stream) on Red_Ox Pt_1/TiO_2 with a series of increasingly harsh reduction conditions (increasing reduction time at various temperatures) from left to right. The volcano-shaped curve suggests that the reduction condition needs to be strong enough to activate Pt_1, but too harsh reduction conditions would deactivate them, likely due to sintering. With the optimized reduction condition (H400-30 min), the rWGS reaction rate on Pt_1/TiO_2 is enhanced by 4-fold by the Red_Ox cycle, showing higher activity than Pt_n/TiO_2 predicted by mechanistic studies.[11,12] Meanwhile, we noticed that the Red_Ox-activated Pt_1/TiO_2 experiences minor deactivation during the reaction, to 75−80% of the initial activity after 3 h time-on-stream, rather than the slight

https://doi.org/10.1021/jacsau.1c00111
JACS Au 2021, 1, 977−986

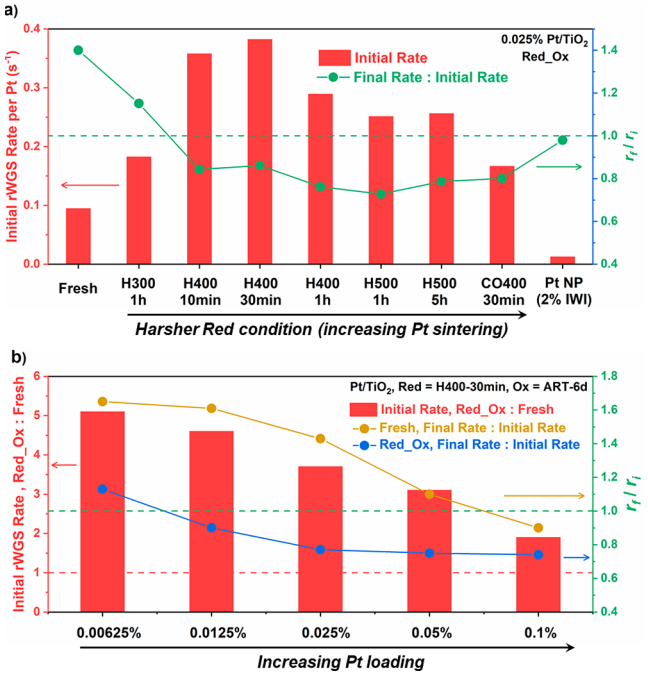

Figure 2. Detailed studies of the Pt_1 activation by the Red_Ox cycle. (a) Efficacy of the cycle with various reduction conditions, with the red bars showing the initial (t = 10 min) rWGS rate per Pt, and the green dots showing the ratio between the final (t = 3 h) and the initial rate on each sample. An optimum in the initial activity exists as the reduction condition becomes harsher. CO is known for its efficacy in mobilizing noble metal atoms,[28−31] and thus CO400-30 min is regarded as a "harsher" condition than H500. (b) The efficacy of the cycle with various Pt loading on TiO_2, with the red bars showing the ratio between the initial rate with and without the cycle, i.e., the activity enhancement level, and the blue/yellow dots showing the ratio between the final and the initial rate on each activated/fresh catalyst. The rWGS conditions are identical with Figure 1b. The complete data used to construct this figure can be found as Figure S3.

activation observed on the fresh sample (green dots in Figure 2a). In contrast, Pt NP/TiO_2 exhibits steady activity. The detailed examination of the deactivation will be presented later, while the rate increase with time-on-stream can serve as a diagnostic for the presence of nonactivated Pt_1. We note that even with the deactivation, the Red_Ox Pt_1/TiO_2 still exhibits clearly higher activity than the fresh catalyst after 40 h time-on-stream (Figure S4).

To further understand the Pt_1 activation, we applied the Red_Ox cycle with the optimal reduction condition (i.e., H400-30 min followed by room-temperature oxidation for 6 days) to a series of Pt/TiO_2 with 0.00625 to 0.1 wt % Pt from the same synthesis method as Pt_1/TiO_2. Since Pt_1/TiO_2 has 0.025 wt % Pt, it is reasonable to assume that at ≤0.025 wt %, all the Pt is atomically dispersed. Literature showed that at >0.025 wt % Pt, atomic Pt dispersion cannot be maintained with this synthesis procedure,[25] consistent with the lack of rate increase with time-on-stream on the fresh catalysts (yellow dots in Figure 2b, representing the ratio between the final and the initial rate on each fresh catalyst, not significantly above 1), the diagnostic for Pt_1. The red bars in Figure 2b, representing the ratio between the initial rate on each catalyst with and without the Red_Ox cycle, i.e., the activity enhancement by the cycle, clearly show that the Red_Ox cycle activates all Pt/TiO_2 catalysts (all bars >1), and its efficacy decreases with increasing Pt loading, consistent with the conclusion that it selectively activates Pt_1 over other Pt species. In addition, among the three SACs, it is more effective with lower Pt_1 surface density, implying that Pt_1 sinter during the cycle, which competes with the activation, consistent with the inference from the volcano-shaped curve in Figure 2a. We note that the blue dots in Figure 2b, representing the ratio between the final and the initial rate on each activated catalyst after 3 h rWGS, show that the reaction rate on the most diluted sample, with 0.00625% Pt, still increases with time-on-stream after the cycle, a sign of incomplete activation. Consequently, if the reduction condition were optimized on this sample, the activity enhancement would exceed 5-fold. In summary, kinetic data indicate that the Red_Ox cycle selectively activates Pt_1, which is required to uncover the superior rWGS activity of Pt_1/TiO_2, and likely competes with Pt sintering under the reducing atmosphere.

2. Elucidating the Mechanism of the Pt_1 Activation

To elucidate the mechanism of the Pt_1 activation, we tracked the structural changes of Pt_1/TiO_2 during the Red_Ox cycle using STEM, XAS, and CO-IR. We chose the optimal reduction condition, H400-30 min in Figure 2a, so if not specified, "Red_Ox" below refers to "H400-30 min_Ox". The oxidation step was conducted under diluted O_2 at 250 °C for ≥6 h. We note that X-ray photoemission spectroscopy (XPS) was attempted but failed to detect Pt on Pt_1/TiO_2, as the loading (0.025 wt %, ∼0.01 at. %) is below the detection limit of Pt on TiO_2 in literature (∼0.1 at. %).[32]

STEM images of the Pt_1/TiO_2 catalyst treated under different conditions are shown in Figure 3 (see Figure S5 for

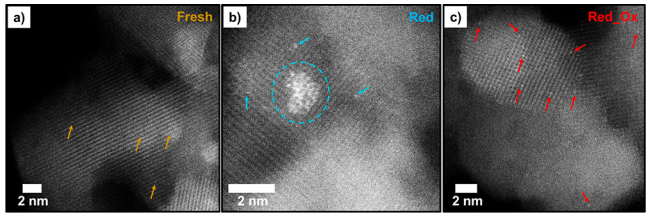

Figure 3. HAADF-STEM images of 0.025% Pt/TiO_2 (Pt_1/TiO_2): (a) fresh sample; (b) after 4% H_2 reduction at 400 °C for 30 min and immediately transferred into the vacuum; (c) after 20% O_2 oxidation at 250 °C for 12 h following the reduction. All arrows point to Pt single atoms, and dashed circle in (b) highlights one of the Pt aggregates. Additional images can be found in Figure S5a−c to show that the images are representative. Line-scan analysis of the fresh and the Red_Ox catalysts can be found as Figure S5d, e, respectively, to further confirm that Pt species are mononuclear on both samples.

additional images and line-scan analysis). The fresh catalyst shows exclusively Pt single atoms, proving the atomic dispersion of Pt (Figure 3a). After the reduction, the sample was immediately transferred to vacuum for imaging with minimal air exposure. A small number of Pt aggregates with ∼1 nm diameter were identified, along with Pt single atoms (Figure 3b). The aggregates do not resemble typical Pt nanoparticles: they lack three-dimensional structures and Pt atoms at the peripheral positions seem loosely connected to others and were observed to move during imaging. Therefore, these features are likely amorphous, mobile, and loosely bound Pt aggregates, visually resembling Pt 2D-rafts reported on Al_2O_3.[33] After the entire Red_Ox cycle, we observed only Pt single atoms again with no evidence of Pt aggregates (Figure

https://doi.org/10.1021/jacsau.1c00111
JACS Au 2021, 1, 977−986

3c). Consequently, STEM reveals that Pt_1 experience minor aggregation during the reduction, but are redispersed into Pt_1 during the reoxidation.

Figure 4 summarizes the Pt L_3-edge XAS results. EXAFS data were analyzed by modeling (Figure 4a, showing Fourier

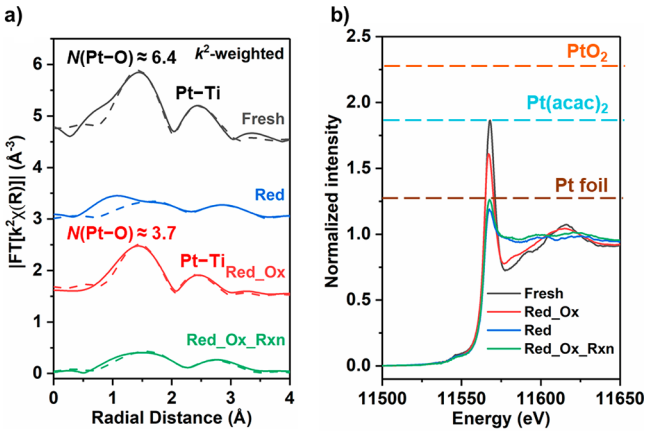

Figure 4. Pt L_3-edge XAS results on Pt_1/TiO_2: (a) the EXAFS (*R*-space magnitude, best fitting shown as dashed curves, each spectrum offset by 1.5); (b) the XANES. The spectra were collected at room temperature on the same sample in sequence after each step: black, fresh; blue, after reduction; red, after reoxidation; green, after 250 °C rWGS reaction. The EXAFS fitting parameters are listed in Table S2, and supplemental analysis results can be found in Figures S6−S8. Dashed lines in b show the white-line intensity of Pt standards with 0 (Pt foil), + 2 ($Pt(acac)_2$), and +4 (PtO_2) Pt oxidation state for comparison.

transformation in *R*-space magnitude with fittings as dashed lines, the imaginary part and *k*-space data as shown in Figure S6) and wavelet transformation (WT, Figure S8). For the fresh catalyst (black), the best EXAFS model was obtained using both a Pt−O scattering path and a Pt−Ti path. For comparison, replacing the Pt−Ti path with a Pt−Pt path from either Pt metal or PtO_2 leads to poor agreement with the data (Figure S7a). In addition, WT (Figure S8a) shows that the intensity between nonphase resolved 2 and 3 Å is localized in a different *k* range from Pt−Pt (3−7 $Å^{-1}$ compared to 8−12 $Å^{-1}$ in Figure S8e, f) that is consistent with lower atomic number element than Pt, such as Ti. Therefore, we conclude that as the EXAFS has negligible contribution from Pt−Pt, the Pt is predominantly atomically dispersed. Figure 4a and Table S2 also show that the fresh catalyst has high coordination number (*N*) of Pt−O, 6.4 ± 0.4, i.e., the Pt_1 are highly O-coordinated. In fact, the *N*(Pt−O) and *N*(Pt−Ti) = 4.7 ± 0.6 are close to *N*(Ti−O) = 6 and *N*(Ti−Ti) = 4 in anatase respectively, implying a probable scenario that most Pt substitute a Ti in the lattice, sitting in a coordination-saturated environment. Meanwhile, in the XANES region, the white-line intensity of Pt_1/TiO_2 (Figure 4b, black) is similar to the Pt(II) standard $Pt(acac)_2$ and significantly higher than Pt foil, suggesting that the Pt_1 are clearly cationic.

After the reduction, the EXAFS changes significantly (Figure 4a, blue). Three paths are now required for the best fit model (Table S2): a Pt−O path, a metallic Pt−Pt path, and the same Pt−Ti path. Models without the Pt−Pt path fail to adequately account for the intensity between 2 and 3 Å (Figure S7c). In addition, WT (Figure S8c) suggests that the intensity between 2 and 2.5 Å has contribution from scatterers with high atomic numbers such as Pt. The presence of a metallic Pt−Pt scattering path is consistent with the observation of some Pt aggregates in STEM, and the significantly lower average *N*(Pt−O) = 1.1 ± 0.4 is consistent with Pt_n clusters bound to the TiO_2 support. Besides, in the XANES region, the white-line intensity decreases as expected after the reduction, to approximately that of Pt foil (Figure 4b, blue), indicating that the Pt is mostly metallic, also consistent with Pt aggregation. Furthermore, the mean square deviation in half-path length (σ^2) of the Pt−Pt path (0.017 ± 0.007) in the best fitting is higher than normal values for crystalline Pt (e.g., 0.005 ± 0.003 for Pt foil in Table S3), implying some disorder in the Pt−Pt bonds in the small clusters and leading to the visually weak EXAFS intensity.

After the reoxidation, the EXAFS (Figure 4a, red) changes back to resemble the fresh catalyst qualitatively: it is also best fit with the same Pt−O and Pt−Ti paths (Table S2), replacing the Pt−Ti path with either Pt−Pt path leads to worse fittings (Figure S7b), and WT (Figure S8b) indicates that the intensity between 2 and 3 Å is from lighter scatterers than Pt. Therefore, the Pt is again atomically dispersed. Nonetheless, the scattering is visibly weaker than in the fresh catalyst, and the fitting shows significantly lower *N*(Pt−O) and *N*(Pt−Ti), i.e., 3.7 ± 0.9 and 2.2 ± 0.7 compared to 6.4 ± 0.4 and 4.7 ± 0.6 (Table S2). In addition, the white-line intensity recovers (Figure 4b, red) from the postreduction sample, but is lower than the fresh catalyst. These results suggest that these Pt_1 are in a less O-coordinated environment than the Pt_1 on the fresh catalyst, with lower average oxidation state. Overall, XAS confirms that Pt_1 aggregate during the reduction, and are redispersed into Pt_1 during the reoxidation. It further shows that the redispersed Pt_1 are in a different chemical environment from the fresh Pt_1.

IR spectra of the Pt_1/TiO_2 catalyst after room-temperature CO exposure and evacuation are shown in Figure 5 (1700−2300 cm^{-1}, adsorbed CO region, see Figure S9 for spectra

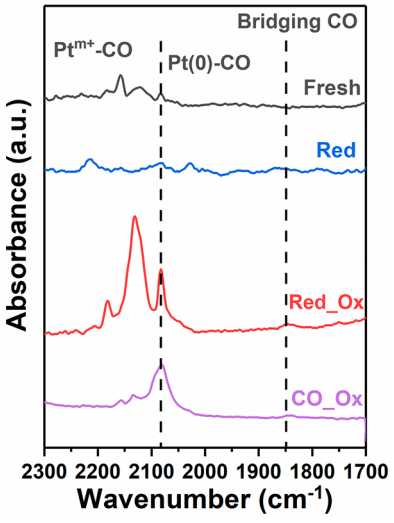

Figure 5. IR spectra of Pt_1/TiO_2 after 0.4 Torr CO exposure at room temperature followed by evacuation. The four spectra represent irreversible CO adsorption (Pt-bound CO) and were collected on the same sample in sequence after each step: black, fresh; blue, after reduction; red, after reoxidation; purple, after CO400−30 min_Ox. All treatments were performed with 1 Torr corresponding gas. Between each two steps, the sample was cleaned by 1 Torr O_2 at 250 °C to eliminate adsorbed CO.

https://doi.org/10.1021/jacsau.1c00111
JACS Au 2021, 1, 977−986

during the evacuation). The fresh sample shows peaks with very low intensities in the region (black), indicating little CO adsorption. Conducting the experiment at 100 K (Figure S10) shows no bands from Pt-bound CO either, eliminating the possibility of CO bound very weakly on Pt. Therefore, Pt on the fresh catalyst have limited accessibility to CO. The weak CO bands are mostly beyond 2100 cm^{-1}, assigned to linear CO on cationic Pt (Pt^{m+}−CO),[34−36] with no bridging CO (1800−1900 cm^{-1}), further confirming the atomic dispersion of Pt. After the reduction, the sample still exhibits limited CO adsorption capacity (blue). Interestingly, after the reoxidation, intense IR bands (red) appear at 2179, 2129, 2121, and 2083 cm^{-1}. The first three features correspond with various types of Pt^{m+}−CO, whereas the latter one is attributed to Pt(0)−CO (there is also a very low-intensity band around 1845 cm^{-1} that could represent CO adsorbed on contiguous Pt sites in a bridging configuration).[34,35] These bands and their intensities suggest that after the Red_Ox cycle (1) the accessibility of Pt to CO significantly increases; (2) most Pt species are positively charged, and the fraction of Pt−Pt sites, i.e., Pt aggregates, is low, even after taking the low IR cross-section of bridging CO on Pt into consideration.[37] The sample was further treated with a CO_Ox cycle (CO400-30 min), which moves it over the peak of the volcano-shaped activity curve in Figure 2a. Afterward, the sample shows adsorbed CO bands at similar positions (purple) with after Red_Ox, but the Pt(0): Pt^{m+} ratio significantly increases, and the total intensity drops, suggesting higher Pt nuclearity. In summary, IR results show the enhanced accessibility of Pt toward CO adsorption after the Red_Ox cycle, further proving the changes in Pt chemical environment suggested by XAS and kinetic data. The results also show that with the optimal reduction condition, Pt remain mostly cationic after the cycle, whereas harsher reduction condition leads to more Pt(0), i.e., larger particles.

3. Deactivation and Oxidative Reactivation of Red_Ox-Activated Pt_1/TiO_2

In the discussion of the kinetic data, we mentioned that the Red_Ox-activated Pt/TiO_2 catalysts experience minor deactivation during the rWGS reaction at 250 °C (Figure 2) or 200 °C (Figure S11a). The deactivation was also observed on Pt_1/TiO_2 after only the reduction and Pt_n/TiO_2 but not on Pt NP/TiO_2 (Table S4), indicating that it is unique to highly dispersed Pt. Further investigation reveals that for activated Pt_1/TiO_2 the deactivation can be fully reversed by exposure to air at room temperature for an extended period of time (7 days, Figure 6a, blue) or by oxidation at 250 °C for short time (30 min, green), but not under an inert atmosphere (He) at high temperature (black). The reactivated Pt_1/TiO_2 exhibits similar deactivation behavior when used again (Figure 6a). In addition, we discovered that at 250 °C, H_2 alone in the rWGS feed cannot induce the deactivation, as the catalyst exhibits identical activity and deactivation with (Figure 6b, blue) and without (red) a 250 °C, 200 min H_2 treatment before the rWGS. In contrast, the deactivation occurs partially under 0.7% CO (brown, identical concentration with that produced in the rWGS stream), and completely under H_2 + CO (black), indicating that the deactivation is caused by the combination of H_2 and CO in the reaction stream but CO is the main contributor.

The resemblance between the oxidation condition leading to the reactivation and in the Red_Ox cycle (air, 250 °C or RT for days) implies similarities between the two processes, i.e., under the rWGS conditions, activated Pt_1 form similar species with fresh Pt_1 during the reduction−the small, amorphous, mobile Pt aggregates. The sintering leads to the deactivation, which can be completely reversed by the oxidative redispersion. XAS of Red_Ox Pt_1/TiO_2 collected after being used for rWGS at 250 °C for 2 h (Figure 4a, green) supports the hypothesis as it resembles XAS of Red Pt_1/TiO_2: damped EXAFS that requires a Pt−Pt path to fit (in addition to Pt−O and Pt−Ti paths, Table S2, and Figure S7c), similarly low N(Pt−O) (1.4 ± 0.3 compared to 1.1 ± 0.4) and high σ^2(Pt−Pt) (0.016 compared to 0.017 ± 0.007), as well as close-to-metallic Pt suggested by XANES (Figure 4b, green). The deactivation is not caused by CO poisoning Pt, because at the experiment temperature of Figure 6 (250 °C), CO completely desorb from TiO_2-supported Pt_1 and mostly desorb from Pt NP.[25,38] Also, Pt NP/TiO_2 does not show such behavior, implying that it originates from the instability of low-nuclearity Pt species. We note that the white-line intensity drop under the rWGS condition completes much faster (in 25 min, Figure S12c) than the deactivation (continuing after 20 h, Figure S4), implying that before aggregation, Pt_1 likely catalyzes the reaction in a reduced but still atomically dispersed state.

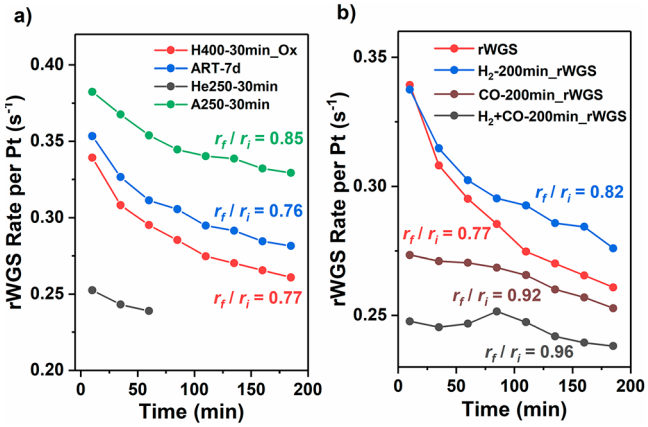

Figure 6. RWGS rate per Pt vs time-on-stream showing the deactivation and oxidative reactivation of the Red_Ox Pt_1/TiO_2. In a, the four curves were measured in sequence on a fresh catalyst following the order and after each treatment in the legends. In b, the red, blue, brown, and black curves were measured after treating an activated catalyst with no treatment, 20% H_2 at 250 °C for 200 min, 0.7% CO at 250 °C for 200 min, and 20% H_2 + 0.7% CO at 250 °C for 200 min, respectively. The rWGS conditions are identical with Figure 1b.

DISCUSSIONS

The combination of kinetic, spectroscopic, and microscopic studies elucidates a clear picture of how the Red_Ox cycle unleashes the rWGS activity of Pt_1/TiO_2 by altering the chemical environment of Pt_1, conceptualized as Figure 7. The coordination sphere of the fresh Pt_1 is saturated with oxygen from TiO_2, evidenced by the high N(Pt−O) ≈ 6 in EXAFS (Figure 4a, Table S2) and low CO adsorption capacity (Figure 5). The match between the EXAFS data and the Ti-substitution model implies that each Pt_1 substitute a Ti in TiO_2, and thus are in the surface layer or subsurface instead of on the surface. The chemical environment predicts low Pt accessibility, as shown by the lack of Pt−CO bands in IR, rationalizing the low rWGS activity. Single noble metal atoms in similar substitutional environment have been reported

https://doi.org/10.1021/jacsau.1c00111
JACS Au 2021, 1, 977−986

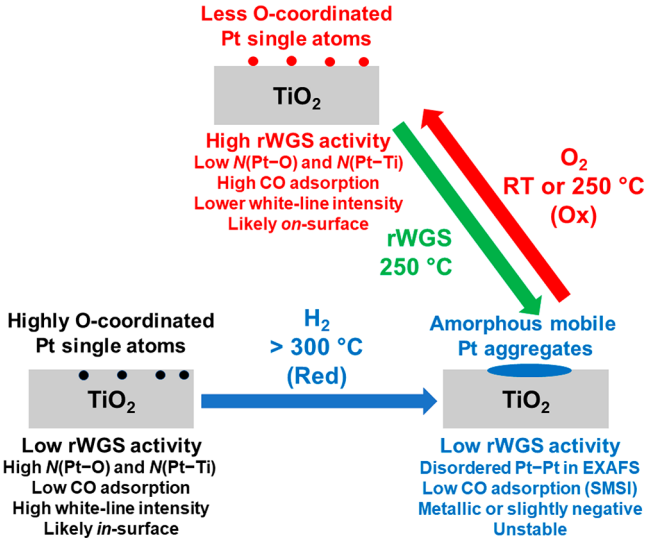

Figure 7. Summary of the evolution of Pt_1/TiO_2 during the Red_Ox activation cycle.

before on TiO_2.[18,19] We note that the white-line intensity is known to be affected by the coordination environment of the metal centers, in addition to their oxidation state.[39−42] Therefore, we refrained from concluding Pt oxidation state solely based on XANES. In fact, the white-line intensity of the fresh Pt_1 is close to $Pt(acac)_2$, but the Ti-substitution model suggested by the EXAFS predicts +4 oxidation state, emphasizing the cautious one should take in determining oxidation state from the white-line intensity. We also note that Christopher et al. reported a 2135 cm^{-1} CO-IR band on Pt_1/TiO_2 observed only at <−50 °C and assigned it to weakly bound Pt^{m+}−CO.[18] Nevertheless, even at 100 K, we did not observe any bands of adsorbed CO besides ones on pristine anatase TiO_2 (2128 and 2137 cm^{-1} in Figure S10), i.e., there is no weakly bound Pt^{m+}−CO. Besides, the weak Pt^{m+}−CO bands on the fresh Pt_1/TiO_2 in Figure 5 are located at various positions, suggesting that Pt_1 are not completely uniform, also different from results from Christopher et al.[18,25] Therefore, the fresh Pt_1/TiO_2 in the two studies are not identical.

The reduction step hydroxylates and cleaves Pt−O bonds, as suggested by the decreased N(Pt−O) in EXAFS and shown by mechanistic studies,[11,12] mobilizing Pt_1. Pt could hence aggregate, but the formation of large, stable particles can be avoided by carefully controlling the reduction condition, so that only small, amorphous, loosely bound, and mobile Pt aggregates are formed, as observed in STEM (Figure 3b) and consistent with the high degree of disorder in the Pt−Pt scattering path. The volcano-shaped activity curve (Figure 2a) shows the delicate balance in the reduction step: too mild condition would fail to cleave Pt−O bonds and thus activate Pt_1 (e.g., H300-1h_Ox catalyst shows low activity and rate increase with time-on-stream, signs of incomplete Pt_1 activation), whereas too harsh condition would create large and stable Pt particles that cannot be redispersed by the reoxidation applied (e.g., CO400-30 min_Ox catalyst shows also low activity and mostly zero-valence Pt). We note that Pt aggregates after the reduction visually resemble 2D rafts, the stabilization of which in similar systems was attributed to support-to-metal electron transfer.[17,33,43−47] Actually, we observed slightly lower Pt white-line intensity than Pt foil (Figure 4b), so the Pt single atoms and small clusters could carry partial negative charges. Nevertheless, the Pt−Ti distance (3.04 ± 0.06 Å) is consistent with a Pt−O−Ti structure, not direct M_1−Ti bonds (~2.5 Å) at oxygen vacancies (O_v) reported on defective rutile TiO_2.[17,47] Therefore, there is no direct contact between Pt and Ti cations, likely a result of surface O_v on anatase being less favored than subsurface O_v.[48−50] Meanwhile, the 250 °C oxidation does not redisperse Pt clusters on Pt_n/TiO_2 (Figure S11c), highlighting the difference between Pt aggregates created from Pt_1 reduction and those synthesized by wet chemistry methods. In addition, the catalyst after the reduction exhibit strong metal−support interaction (SMSI), implied by the lack of CO adsorption (Figure 5), which may also be responsible for the low rWGS activity at this stage (Figure 1b) along with the decreased Pt dispersion.

The reoxidation step completes the activation by redispersing Pt into Pt_1. Nonetheless, compared to the fresh Pt_1, the redispersed, i.e., activated, Pt_1 are not coordinately saturated with oxygen, evidenced by lower N(Pt−O) and N(Pt−Ti) in EXAFS (Figure 4a, Table S2), as well as significantly higher CO adsorption capacity (Figure 5). These characteristics imply that Pt_1 migrate from the TiO_2 surface layer (in-surface) or subsurface to the surface (on-surface). The increased accessibility and coordination vacancies of Pt_1 logically predict higher rWGS activity, reflected by the kinetic data. Also, the less O-coordinated environment is consistent with the lower XANES white-line intensity (Figure 4b). Anatase TiO_2 is oxidized at this point, and no direct Pt−Ti bonds are suggested by the EXAFS. Therefore, the activated Pt_1 are not likely anchored by surface defects. We note that in STEM, activated Pt_1 (Figure 3c) appear brighter than fresh Pt_1 (Figure 3a), which could be due to Pt migration onto the surface as well (different TiO_2 thickness might also lead to the observation). We also note that in CO-IR, Red_Ox Pt_1/TiO_2 shows a very weak bridging CO band (Figure 5), despite that both STEM and EXAFS show atomic Pt dispersion. This could be due to the different O_2 pressure applied during the reoxidation: 1 Torr in CO-IR compared to ~150 Torr in the other two. This scheme predicts that the reducing rWGS condition would be equivalent with a reduction step, validated by kinetic data in Figure 1 showing that the reaction activates fresh Pt_1, and the qualitatively similar XAS of R250-13h_Ox and H400-30 min_Ox catalysts (Figure S13).

Because previous mechanistic studies clearly showed that the rWGS always follows the carboxyl pathway on supported noble metal catalysts at the metal−support interface (rather than continuous metal sites, and formates are spectators), regardless of metal nuclearity or support identity,[11,12] the rWGS is expected to follow the same mechanism on Pt_1/TiO_2 with or without the Red_Ox cycle. In fact, when the rate is stabilized on fresh and Red_Ox Pt_1/TiO_2, the E_a and the reaction rate dependence on H_2 and CO_2 partial pressures are all similar (Figure S14), supporting an identical reaction mechanism. Therefore, the activity enhancement is mainly due to the higher chance that such chemistry occurs at the interfacial active sites, as Pt_1 become more accessible to the reactants (indicated by the enhanced accessibility to CO in Figure 5). This is reflected by the increase in the pre-exponential factor on the activated Pt_1/TiO_2 (Figure S14). Besides, theoretical calculation suggested that metal sites activate CO_2 and stabilize carboxyl more effectively when less coordinated and more negatively charged. Consequently, the lower Pt coordination

https://doi.org/10.1021/jacsau.1c00111
JACS Au 2021, 1, 977−986

number (EXAFS) and white-line intensity (XANES) after the activation imply potentially higher CO_2 activation efficiency.

The optimal Red_Ox cycle boosts the per-Pt rWGS rate on Pt_1/TiO_2 to 0.4 s^{-1} at 250 °C, clearly higher than Pt_n/TiO_2 (0.2 s^{-1}, Figure S11b), consistent with mechanistic studies claiming metal-oxide interfacial active sites.[11,12] The activation mechanism emphasizes the importance of the metal−support interaction on SACs: it is crucial to stabilize single atoms, but the support can saturate the metal coordination sphere, leading to the loss of catalytic activity. Christopher et al. reported that 450 °C H_2 reduction leads to more active Pt_1 for CO oxidation.[18] Sautet et al. reported the interchange between substitutional and supported Rh_1 on TiO_2 under various rWGS conditions affecting activity, both resonating with this work.[19] These limited examples show that the dynamic responses of metal single atoms to the atmospheres, which are often undesired as they cause catalyst instability and complicate the reaction, could be a blessing in disguise—they can be utilized to maximize the catalytic potential of single atoms by manipulating their bonding with the support and thus chemical environment.

Our results also indicate that during 250 °C rWGS, activated Pt_1 transforms gradually into Pt aggregates similar to those formed during the initial reduction, reversibly deactivating Pt_1/TiO_2. At 250 °C, H_2 + CO is required for the aggregation to proceed slowly (Figure S4), whereas at ≥400 °C during the reduction, CO is not necessary and only ≤1 h of time is required. The dynamic Pt_1/aggregates interchange by oxidation/reduction emphasizes the necessity of tracking the operando catalyst structural evolution to understanding single-atom catalysis accurately. In addition, as the thermodynamics of single atoms is predominately determined by the metal−support bonds, the M−O cleavage under harsh reducing conditions inevitably destabilizes them. This issue poses significant challenges to using SACs for high-temperature hydrogenation reactions, resulting in very scarce reports beyond this work.[16,17] This is further aggravated with CO involved as the reactant or even low-concentration product (such as in this work), which leads to mobile metal carbonyl and facilitates sintering. Consequently, the oxidative redispersion under mild conditions (room-temperature air) reported here offers a potential strategy to effectively alleviate the problem and thus expand the application scope of SACs.

CONCLUSIONS

Here we report on a reduction−oxidation cycle that selectively activates Pt single atoms on anatase TiO_2, achieving optimal activity for the reverse water−gas shift (rWGS) reaction. The activation mechanism was revealed by systematic kinetic, STEM, CO-IR, and XAS studies. After calcination, the catalyst contains highly O-coordinated Pt single atoms with limited accessibility and coordination vacancies to participate in catalysis, consequently exhibiting unexpectedly low rWGS rate. During the reduction step (H_2, >300 °C), the interruption of Pt−O−Ti bonds leads to small, amorphous, mobile Pt aggregates, which are unstable and redispersed in the following reoxidation step (air, RT or 250 °C) into single atoms. These newly formed Pt single atoms are less O-coordinated and more accessible, therefore showing significantly higher rWGS rate. Careful control of the reduction condition is required to cleave Pt−O bonds, mobilizing Pt while avoiding the formation of (large) Pt particles too stable for the redispersion. Besides, the activated Pt/TiO_2 SAC shows slow deactivation, but is completely reactivated by reoxidation under mild conditions. This work shows that properly manipulating the chemical environment of supported single atoms and their interaction with the support can maximize their catalytic efficiency. It also provides valuable insights to the dynamic behaviors of SACs under pretreatment and reaction conditions as well as their catalytic consequences.

EXPERIMENTAL SECTION

Catalyst Synthesis

Pt/TiO_2 catalysts were synthesized following a strong electrostatic adsorption procedure. Twenty milliliters of a NH_4OH (Sigma-Aldrich, 28.0−30.0% NH_3 basis) solution of the proper amount of $Pt(NH_3)_4(NO_3)_2$ (Sigma-Aldrich, 99.995%) was added to 75 mL of NH_4OH + 25 mL of H_2O + 1 g of anatase TiO_2 (US Research Nanomaterials, 99.5%, 5 nm) under a 500 rpm stirring at a rate addition of 1.2 mL/h. The solid was centrifuged, dried at 70 °C, and calcined under static air at 400 °C for 4 h, resulting in the fresh catalysts. For Pt_n/TiO_2, TiO_2 was calcined at 800 °C for 6 h prior to the synthesis to reduce its surface area and thus Pt dispersion. Pt NP/TiO_2 was synthesized by incipient wetness impregnation with anatase TiO_2 and $Pt(NH_3)_4(NO_3)_2$ at 2 wt % Pt loading.

Catalyst Treatment and rWGS Testing

The treatment and testing of Pt/TiO_2 catalysts for the rWGS were conducted in a fixed bed tubular quartz reactor in a tube furnace. A thermocouple was placed just above the bed to monitor temperature. The treatment was conducted with 20% H_2, 2% CO, or air at ambient pressure. For typical rWGS testing, the reactor loaded with 30 mg of Pt/TiO_2 and 170 mg of SiO_2 was heated to 250 °C under He (40 °C/min). Then gas feed composition was switched to CO_2:H_2:He = 1:4:15 with a total flow rate of 40 SCCM vented to atmosphere. Reaction progress was assessed using an online gas chromatography (Agilent 7890B with a Supelco Carboxen 1010 PLOT column, methanizer, and FID detector). The GC was run under isothermal conditions (35 °C) for 25 or 60 min using He carrier (10 mL/min). The retention times of CO and CO_2 were 2.4 and 13.9 min, respectively. For the kinetic parameter measurements, one of either the temperature, H_2 concentration, or CO_2 concentration was varied accordingly while the others were kept constant.

Catalyst Characterization

High-Angle Annular Dark-Field Scanning Transmission Electron Microscopy (HAADF-STEM). Atomic resolution HAADF-STEM imaging of the Pt/TiO_2 catalyst were acquired using a probe corrected JEOL NeoARM STEM operating at 200 kV.

X-ray Absorption Spectroscopy (XAS). XAS measurements at Pt L3-edge (11.564 keV) were performed at beamline 9−3 of the Stanford Synchrotron Radiation Lightsource at the SLAC National Laboratory. Beamline 9−3 is a 16-pole, 2-T wiggler beamline with a vertically collimating mirror for harmonic rejection and a cylindrically bent mirror for focusing. Incident photon energy was selected by the liquid N_2-cooled, double-crystal Si(220) monochromator at crystal orientation of $\varphi = 90°$. Approximately 35 mg of the Pt_1/TiO_2 catalyst was loaded to make a 10 mm bed in a 3 mm quartz tube flow-through reactor.[51] The reactor was mounted on the sample stage at a 45° angle relative to the X-ray beam. Spectra were collected in fluorescence detection mode using a 100-element germanium detector orthogonal (90°) to the beam path with a Soller slit and Zn filter (absorption length of 3). The beam size of 1 mm [v] by 4 mm [h] was used. N_2-filled ion chambers were used to measure the incident X-ray intensity. A Pt foil was scanned simultaneously with the sample for energy calibration using a photodiode at an off-axis angle because the sample was blocking the X-ray beam. In situ EXAFS measurements, consisting of nine scans, were collected at room temperature under He for the fresh catalyst and under corresponding treatment gas after reduction (20% H_2/He, 400 °C, 30 min), reoxidation (20%O_2/He, 250 °C, 6 h), and the rWGS reaction (20% H_2/5% CO_2/He, 250 °C, 2 h). Spectra in the XANES region were continuously collected

https://doi.org/10.1021/jacsau.1c00111
JACS Au 2021, 1, 977−986

throughout each treatment step. Gas flow rates were controlled using mass flow controllers (Brooks) and temperature was controlled with a Eurotherm PID controller. To monitor the gas flows, we used a mass-spectrometer (Hiden QGA) throughout the experiment. For the ex situ EXAFS measurement of the R250−13h_Ox catalyst, the powder sample was pressed into a 3 mm thick pellet and was encapsulated between two layers of Kapton tape. The pellet was mounted on a sample holder at 45° angle relative to the X-ray beam, and 25 spectra were collected in fluorescence mode using the same detector setup used for the in situ experiment as described above.

EXAFS oscillations were extracted using Athena code and analyzed using Artemis software.[52] A Ti atom was replaced by a Pt atom in anatase TiO_2 structure to calculate the Pt−O and Pt−Ti scattering paths using FEFF. Two Pt−Pt paths were calculated from Pt foil and PtO_2 models, respectively. A Pt−O path was also calculated from the PtO_2 model. The amplitude reduction factor (S_0^2) was found for the Pt foil and fixed for the samples as 0.82 (Table S3). The photoelectron energy origin correction (ΔE_0) was set identical for all scattering paths of the same sample. The k range for the Fourier transformation was selected as 3−8 $Å^{-1}$ to filter out high-k noise that creates artificial scattering intensity in R-space between 1 and 1.5 $Å^{-1}$. Continuous Cauchy Wavelet Analysis (WT) analysis was performed with the EXAFS spectra. WT analysis is interesting to correlate coordination atom shells that have the similar bond distance but yields backscattering contributions coming from different k intervals, especially when different elements are involved.[53] In this case, a better evaluation of Pt−Ti, Pt−Pt from Pt_1 and Pt_n clusters and Pt−Pt from PtO_2 can be attained. WT analysis was performed using k^2-weight EXAFS spectra in a range of k = 2.0−12 $Å^{-1}$, with a Cauchy order of n = 200.

CO-Adsorption Infrared Spectroscopy (CO-IR). CO-IR experiments were performed in a vacuum chamber with a Bruker Vertex 80 IR spectrometer. The sample pellet was supported on a tungsten grid. The system was baked overnight, and then the sample was cleaned by 1 Torr O_2 at 400 °C for 10 min. All treatments were performed with 1 Torr of the desired gas. For a typical measurement, the sample was exposed to 0.4 Torr CO at room temperature after background collection, and CO was then evacuated with continuous spectrum collection. The sample was cleaned by 1 Torr O_2 at 250 °C for 5 min to eliminate adsorbed CO before next treatment. For low-temperature measurements, the sample was cooled by liquid N_2 to ∼100 K during the CO exposure evacuation.

■ ASSOCIATED CONTENT

Supporting Information

The Supporting Information is available free of charge at https://pubs.acs.org/doi/10.1021/jacsau.1c00111.

XRD and BET of the anatase TiO_2 support treated at various temperatures; characterization of Pt_n/TiO_2 and Pt NP/TiO_2; complete and supplemental rWGS kinetic data; additional STEM images; supplemental XAS data (transient XANES, R250-13h_Ox Pt_1/TiO_2) and analysis (comparing fitting strategies and WT); supplemental CO-IR data; summary of the catalyst deactivation; plots for the E_a and reaction order measurements (PDF)

■ AUTHOR INFORMATION

Corresponding Author

Janos Szanyi − *Institute for Integrated Catalysis, Pacific Northwest National Laboratory, Richland, Washington 99352, United States;* orcid.org/0000-0002-8442-5465; Email: Janos.Szanyi@pnnl.gov

Authors

Linxiao Chen − *Institute for Integrated Catalysis, Pacific Northwest National Laboratory, Richland, Washington 99352, United States*

Raymond R. Unocic − *Center for Nanophase Materials Science, Oak Ridge National Laboratory, Oak Ridge, Tennessee 37831, United States;* orcid.org/0000-0002-1777-8228

Adam S. Hoffman − *Stanford Synchrotron Radiation Lightsource, SLAC National Accelerator Laboratory, Menlo Park, California 94025, United States*

Jiyun Hong − *Stanford Synchrotron Radiation Lightsource, SLAC National Accelerator Laboratory, Menlo Park, California 94025, United States*

Adriano H. Braga − *Institute of Chemistry, University of São Paulo, São Paulo, São Paulo 05508-000, Brazil;* orcid.org/0000-0003-4227-6550

Zhenghong Bao − *Chemical Sciences Division, Oak Ridge National Laboratory, Oak Ridge, Tennessee 37831, United States*

Simon R. Bare − *Stanford Synchrotron Radiation Lightsource, SLAC National Accelerator Laboratory, Menlo Park, California 94025, United States*

Complete contact information is available at: https://pubs.acs.org/10.1021/jacsau.1c00111

Notes

The authors declare no competing financial interest.

■ ACKNOWLEDGMENTS

This work was supported by the U.S. Department of Energy (DOE), Office of Science, Office of Basic Energy Sciences, Division of Chemical Sciences, Geosciences and Biosciences, and performed at the Environmental Molecular Sciences Laboratory in (EMSL), which is a DOE Office of Science User Facility located at Pacific Northwest National Laboratory (PNNL). PNNL is a multiprogram national laboratory operated for DOE by Battelle. We acknowledge Dr. Mark E. Bowden, X. Shari Li, and Dr. Libor Kovarik at PNNL for XRD, BET, and supplemental STEM measurements. STEM imaging in the manuscript was conducted at the Center for Nanophase Materials Sciences, which is a DOE Office of Science User Facility. Use of the Stanford Synchrotron Radiation Lightsource, SLAC National Accelerator Laboratory, is supported by the U.S. Department of Energy, Office of Science, Office of Basic Energy Sciences, under Contract DE-AC02-76SF00515. Co-ACCESS is supported by the U.S. Department of Energy, Office of Basic Energy Sciences, Chemical Sciences, Geosciences and Bioscience Division. This research used resources of the Advanced Photon Source (APS), an Office of Science User Facility operated for the U.S. Department of Energy (DOE) Office of Science by Argonne National Laboratory, and was supported by the U.S. DOE under Contract DE-AC02-06CH11357, and the Canadian Light Source and its funding partners. We acknowledge Dr. Debora Meira at the APS for supplemental XAS measurements. A.H.B. acknowledges RCGI − Research Centre for Gas Innovation, hosted by the University of São Paulo (USP) and sponsored by FAPESP−São Paulo Research Foundation (2014/50279-4) and Shell Brasil.

REFERENCES

(1) Álvarez, A.; Bansode, A.; Urakawa, A.; Bavykina, A. V.; Wezendonk, T. A.; Makkee, M.; Gascon, J.; Kapteijn, F. Challenges in the Greener Production of Formates/Formic Acid, Methanol, and DME by Heterogeneously Catalyzed CO_2 Hydrogenation Processes. *Chem. Rev.* **2017**, *117* (14), 9804−9838.

(2) Rodriguez, J. A.; Evans, J.; Feria, L.; Vidal, A. B.; Liu, P.; Nakamura, K.; Illas, F. CO_2 hydrogenation on Au/TiC, Cu/TiC, and Ni/TiC catalysts: Production of CO, methanol, and methane. *J. Catal.* **2013**, *307*, 162−169.

(3) Kijeński, J.; Winiarek, P.; Paryjczak, T.; Lewicki, A.; Mikołajska, A. Platinum deposited on monolayer supports in selective hydrogenation of furfural to furfuryl alcohol. *Appl. Catal., A* **2002**, *233* (1), 171−182.

(4) Lou, Y.; Zheng, Y.; Li, X.; Ta, N.; Xu, J.; Nie, Y.; Cho, K.; Liu, J. Pocket-like active site of Rh_1/MoS_2 single-atom catalyst for selective crotonaldehyde hydrogenation. *J. Am. Chem. Soc.* **2019**, *141*, 19289.

(5) Zhang, L.; Zhou, M.; Wang, A.; Zhang, T. Selective Hydrogenation over Supported Metal Catalysts: From Nanoparticles to Single Atoms. *Chem. Rev.* **2020**, *120* (2), 683−733.

(6) Ratnasamy, C.; Wagner, J. P. Water Gas Shift Catalysis. *Catal. Rev.: Sci. Eng.* **2009**, *51* (3), 325−440.

(7) Reddy, G.; Smirniotis, P. Mechanism and Kinetics of the WGS Reaction. In *Water Gas Shift Reaction*; Elsevier: Amsterdam, 2015; pp 225−261.

(8) Kwak, J. H.; Kovarik, L.; Szanyi, J. CO_2 Reduction on Supported Ru/Al2O3 Catalysts: Cluster Size Dependence of Product Selectivity. *ACS Catal.* **2013**, *3* (11), 2449−2455.

(9) Matsubu, J. C.; Yang, V. N.; Christopher, P. Isolated Metal Active Site Concentration and Stability Control Catalytic CO_2 Reduction Selectivity. *J. Am. Chem. Soc.* **2015**, *137* (8), 3076−3084.

(10) Li, S.; Xu, Y.; Chen, Y.; Li, W.; Lin, L.; Li, M.; Deng, Y.; Wang, X.; Ge, B.; Yang, C.; Yao, S.; Xie, J.; Li, Y.; Liu, X.; Ma, D. Tuning the Selectivity of Catalytic Carbon Dioxide Hydrogenation over Iridium/Cerium Oxide Catalysts with a Strong Metal-Support Interaction. *Angew. Chem., Int. Ed.* **2017**, *56* (36), 10761−10765.

(11) Nelson, N. C.; Nguyen, M.-T.; Glezakou, V.-A.; Rousseau, R.; Szanyi, J. Carboxyl intermediate formation via an in situ-generated metastable active site during water-gas shift catalysis. *Nat. Catal.* **2019**, *2* (10), 916−924.

(12) Nelson, N. C.; Szanyi, J. Heterolytic Hydrogen Activation: Understanding Support Effects in Water-Gas Shift, Hydrodeoxygenation, and CO Oxidation Catalysis. *ACS Catal.* **2020**, *10*, 5663−5671.

(13) Yang, X.-F.; Wang, A.; Qiao, B.; Li, J.; Liu, J.; Zhang, T. Single-Atom Catalysts: A New Frontier in Heterogeneous Catalysis. *Acc. Chem. Res.* **2013**, *46* (8), 1740−1748.

(14) Chen, Y.; Huang, Z.; Ma, Z.; Chen, J.; Tang, X. Fabrication, characterization, and stability of supported single-atom catalysts. *Catal. Sci. Technol.* **2017**, *7* (19), 4250−4258.

(15) Cui, X.; Li, W.; Ryabchuk, P.; Junge, K.; Beller, M. Bridging homogeneous and heterogeneous catalysis by heterogeneous single-metal-site catalysts. *Nat. Catal.* **2018**, *1* (6), 385−397.

(16) Huang, F.; Deng, Y.; Chen, Y.; Cai, X.; Peng, M.; Jia, Z.; Ren, P.; Xiao, D.; Wen, X.; Wang, N.; Liu, H.; Ma, D. Atomically Dispersed Pd on Nanodiamond/Graphene Hybrid for Selective Hydrogenation of Acetylene. *J. Am. Chem. Soc.* **2018**, *140* (41), 13142−13146.

(17) Nelson, N. C.; Chen, L.; Meira, D.; Kovarik, L.; Szanyi, J. In Situ Dispersion of Palladium on TiO_2 During Reverse Water-Gas Shift Reaction: Formation of Atomically Dispersed Palladium. *Angew. Chem., Int. Ed.* **2020**, *59* (40), 17657−17663.

(18) DeRita, L.; Resasco, J.; Dai, S.; Boubnov, A.; Thang, H. V.; Hoffman, A. S.; Ro, I.; Graham, G. W.; Bare, S. R.; Pacchioni, G.; Pan, X.; Christopher, P. Structural evolution of atomically dispersed Pt catalysts dictates reactivity. *Nat. Mater.* **2019**, *18* (7), 746−751.

(19) Tang, Y.; Asokan, C.; Xu, M.; Graham, G. W.; Pan, X.; Christopher, P.; Li, J.; Sautet, P. Rh single atoms on TiO_2 dynamically respond to reaction conditions by adapting their site. *Nat. Commun.* **2019**, *10* (1), 4488.

(20) Wang, H.; Liu, J.-X.; Allard, L. F.; Lee, S.; Liu, J.; Li, H.; Wang, J.; Wang, J.; Oh, S. H.; Li, W.; Flytzani-Stephanopoulos, M.; Shen, M.; Goldsmith, B. R.; Yang, M. Surpassing the single-atom catalytic activity limit through paired Pt-O-Pt ensemble built from isolated Pt_1 atoms. *Nat. Commun.* **2019**, *10* (1), 3808.

(21) Zhou, X.; Chen, L.; Sterbinsky, G. E.; Mukherjee, D.; Unocic, R. R.; Tait, S. L. Pt-Ligand single-atom catalysts: tuning activity by oxide support defect density. *Catal. Sci. Technol.* **2020**, *10* (10), 3353−3365.

(22) Tian, S.; Gong, W.; Chen, W.; Lin, N.; Zhu, Y.; Feng, Q.; Xu, Q.; Fu, Q.; Chen, C.; Luo, J.; Yan, W.; Zhao, H.; Wang, D.; Li, Y. Regulating the Catalytic Performance of Single-Atomic-Site Ir Catalyst for Biomass Conversion by Metal-Support Interactions. *ACS Catal.* **2019**, *9* (6), 5223−5230.

(23) Hu, P.; Huang, Z.; Amghouz, Z.; Makkee, M.; Xu, F.; Kapteijn, F.; Dikhtiarenko, A.; Chen, Y.; Gu, X.; Tang, X. Electronic Metal-Support Interactions in Single-Atom Catalysts. *Angew. Chem., Int. Ed.* **2014**, *53* (13), 3418−3421.

(24) Han, B.; Guo, Y.; Huang, Y.; Xi, W.; Xu, J.; Luo, J.; Qi, H.; Ren, Y.; Liu, X.; Qiao, B.; Zhang, T. Strong Metal-Support Interactions between Pt Single Atoms and TiO_2. *Angew. Chem., Int. Ed.* **2020**, *59* (29), 11824−11829.

(25) DeRita, L.; Dai, S.; Lopez-Zepeda, K.; Pham, N.; Graham, G. W.; Pan, X.; Christopher, P. Catalyst Architecture for Stable Single Atom Dispersion Enables Site-Specific Spectroscopic and Reactivity Measurements of CO Adsorbed to Pt Atoms, Oxidized Pt Clusters, and Metallic Pt Clusters on TiO_2. *J. Am. Chem. Soc.* **2017**, *139* (40), 14150−14165.

(26) Zhang, H.; Banfield, J. F. Thermodynamic analysis of phase stability of nanocrystalline titania. *J. Mater. Chem.* **1998**, *8* (9), 2073−2076.

(27) Patra, S.; Davoisne, C.; Bouyanfif, H.; Foix, D.; Sauvage, F. Phase stability frustration on ultra-nanosized anatase TiO_2. *Sci. Rep.* **2015**, *5* (1), 10928.

(28) Solymosi, F.; Raskó, J. An infrared study of the influence of CO adsorption on the topology of supported ruthenium. *J. Catal.* **1989**, *115* (1), 107−119.

(29) Robbins, J. L. Chemistry of supported Ru: CO-induced oxidation of Ru at 310 K. *J. Catal.* **1989**, *115* (1), 120−131.

(30) Solymosi, F.; Novak, E.; Molnar, A. Infrared spectroscopic study on carbon monoxide-induced structural changes of iridium on an alumina support. *J. Phys. Chem.* **1990**, *94* (18), 7250−7255.

(31) Mizushima, T.; Tohji, K.; Udagawa, Y.; Ueno, A. An EXAFS and IR study of the CO adsorption-induced morphology change in ruthenium catalysts. *J. Am. Chem. Soc.* **1990**, *112* (22), 7887−7893.

(32) Shard, A. G. Detection limits in XPS for more than 6000 binary systems using Al and Mg Kα X-rays. *Surf. Interface Anal.* **2014**, *46* (3), 175−185.

(33) Kwak, J. H.; Hu, J.; Mei, D.; Yi, C.-W.; Kim, D. H.; Peden, C. H. F.; Allard, L. F.; Szanyi, J. Coordinatively Unsaturated Al^{3+} Centers as Binding Sites for Active Catalyst Phases of Platinum on γ-Al_2O_3. *Science* **2009**, *325* (5948), 1670−1673.

(34) Hadjiivanov, K. I.; Klissurski, D. G. Surface chemistry of titania (anatase) and titania-supported catalysts. *Chem. Soc. Rev.* **1996**, *25* (1), 61−69.

(35) Hadjiivanov, K. I. IR study of CO and H_2O coadsorption on Pt^+/TiO_2 and Pt/TiO_2 samples. *J. Chem. Soc., Faraday Trans.* **1998**, *94* (13), 1901−1904.

(36) Primet, M.; Basset, J. M.; Mathieu, M. V.; Prettre, M. Infrared study of CO adsorbed on Pt/Al_2O_3. A method for determining metal-adsorbate interactions. *J. Catal.* **1973**, *29* (2), 213−223.

(37) Vannice, M. A.; Twu, C. C. Extinction coefficients and integrated intensities for linear- and bridged-bonded CO on platinum. *J. Chem. Phys.* **1981**, *75* (12), 5944−5948.

(38) Thang, H. V.; Pacchioni, G.; DeRita, L.; Christopher, P. Nature of stable single atom Pt catalysts dispersed on anatase TiO_2. *J. Catal.* **2018**, *367*, 104−114.

(39) Abbehausen, C.; de Paiva, R. E. F.; Bjornsson, R.; Gomes, S. Q.; Du, Z.; Corbi, P. P.; Lima, F. A.; Farrell, N. X-ray Absorption

https://doi.org/10.1021/jacsau.1c00111
JACS Au 2021, 1, 977−986

Spectroscopy Combined with Time-Dependent Density Functional Theory Elucidates Differential Substitution Pathways of Au(I) and Au(III) with Zinc Fingers. *Inorg. Chem.* **2018**, *57* (1), 218−230.
(40) Chang, S.-Y.; Uehara, A.; Booth, S. G.; Ignatyev, K.; Mosselmans, J. F. W.; Dryfe, R. A. W.; Schroeder, S. L. M. Structure and bonding in Au(I) chloride species: a critical examination of X-ray absorption spectroscopy (XAS) data. *RSC Adv.* **2015**, *5* (9), 6912−6918.
(41) Lei, Y.; Jelic, J.; Nitsche, L. C.; Meyer, R.; Miller, J. Effect of Particle Size and Adsorbates on the L3, L2 and L1 X-ray Absorption Near Edge Structure of Supported Pt Nanoparticles. *Top. Catal.* **2011**, *54* (5), 334−348.
(42) Chen, L.; Ali, I. S.; Sterbinsky, G. E.; Zhou, X.; Wasim, E.; Tait, S. L. Ligand-coordinated Ir single-atom catalysts stabilized on oxide supports for ethylene hydrogenation and their evolution under a reductive atmosphere. *Catal. Sci. Technol.* **2021**, *11* (6), 2081−2093.
(43) Lemire, C.; Meyer, R.; Shaikhutdinov, S. K.; Freund, H. J. CO adsorption on oxide supported gold: from small clusters to monolayer islands and three-dimensional nanoparticles. *Surf. Sci.* **2004**, *552* (1), 27−34.
(44) Sterrer, M.; Risse, T.; Heyde, M.; Rust, H.-P.; Freund, H.-J. Crossover from Three-Dimensional to Two-Dimensional Geometries of Au Nanostructures on Thin MgO(001) Films: A Confirmation of Theoretical Predictions. *Phys. Rev. Lett.* **2007**, *98* (20), 206103.
(45) Risse, T.; Shaikhutdinov, S.; Nilius, N.; Sterrer, M.; Freund, H.-J. Gold Supported on Thin Oxide Films: From Single Atoms to Nanoparticles. *Acc. Chem. Res.* **2008**, *41* (8), 949−956.
(46) Shao, X.; Prada, S.; Giordano, L.; Pacchioni, G.; Nilius, N.; Freund, H.-J. Tailoring the Shape of Metal Ad-Particles by Doping the Oxide Support. *Angew. Chem., Int. Ed.* **2011**, *50* (48), 11525−11527.
(47) Wan, J.; Chen, W.; Jia, C.; Zheng, L.; Dong, J.; Zheng, X.; Wang, Y.; Yan, W.; Chen, C.; Peng, Q.; Wang, D.; Li, Y. Defect Effects on TiO_2 Nanosheets: Stabilizing Single Atomic Site Au and Promoting Catalytic Properties. *Adv. Mater.* **2018**, *30* (11), 1705369.
(48) Li, Y.; Gao, Y. Interplay between Water and TiO_2 Anatase (101) Surface with Subsurface Oxygen Vacancy. *Phys. Rev. Lett.* **2014**, *112* (20), 206101.
(49) Cheng, H.; Selloni, A. Surface and subsurface oxygen vacancies in anatase TiO_2 and differences with rutile. *Phys. Rev. B: Condens. Matter Mater. Phys.* **2009**, *79* (9), 092101.
(50) Cheng, H.; Selloni, A. Energetics and diffusion of intrinsic surface and subsurface defects on anatase TiO_2(101). *J. Chem. Phys.* **2009**, *131* (5), 054703.
(51) Hoffman, A. S.; Singh, J. A.; Bent, S. F.; Bare, S. R. In situ observation of phase changes of a silica-supported cobalt catalyst for the Fischer−Tropsch process by the development of a synchrotron-compatible in situ/operando powder X-ray diffraction cell. *J. Synchrotron Radiat.* **2018**, *25* (6), 1673−1682.
(52) Ravel, B.; Newville, M. ATHENA, ARTEMIS, HEPHAESTUS: data analysis for X-ray absorption spectroscopy using IFEFFIT. *J. Synchrotron Radiat.* **2005**, *12* (4), 537−541.
(53) Galhardo, T. S.; Braga, A. H.; Arpini, B. H.; Szanyi, J.; Gonçalves, R. V.; Zornio, B. F.; Miranda, C. R.; Rossi, L. M. Optimizing Active Sites for High CO Selectivity during CO_2 Hydrogenation over Supported Nickel Catalysts. *J. Am. Chem. Soc.* **2021**, *143* (11), 4268−4280.

https://doi.org/10.1021/jacsau.1c00111
JACS Au 2021, 1, 977−986